Materials Advances

ROYAL SOCIETY OF CHEMISTRY

PAPER

View Article Online
View Journal | View Issue

Cite this: *Mater. Adv.*, 2025, **6**, 6775

Amphiphilic cyclodextrin-based nanocarriers for magnetic delivery of a morphogen in microfluidic environments

Alessandro Surpi, †*[a] Roberto Zagami, †[bc] Marianna Barbalinardo,[a] Nina Burduja,[bc] Giuseppe Nocito,[b] Riccardo Di Corato,[de] Maria Pia Casaletto,[f] Francesco Valle,[a] Angelo Nicosia,[g] Placido Giuseppe Mineo,[g] Valentin Alek Dediu[a] and Antonino Mazzaglia *[b]

Received 17th April 2025,
Accepted 9th August 2025

DOI: 10.1039/d5ma00374a

rsc.li/materials-advances

Reliable methodologies for spatio-temporal controlled delivery of morphogens are of key importance in organoid research, regenerative medicine and developmental biology. To develop such a methodology, we constructed a magnetic nanocarrier composed of a supramolecular nanoassembly of amphiphilic cyclodextrin (SC6OH) entangling superparamagnetic iron oxide nanoparticles (SPIONs) within the surface. Upon encapsulation of a defined amount of retinoic acid (RA), the nanocarriers are remotely guided through microfluidic channels to a cell culture compartment by a specifically designed magnetic device based on electro-mechanically actuated permanent magnets. We demonstrate the efficiency of this innovative technology for the delivery of morphogens by applying it to induce the differentiation of human neuroblastoma SH-SY5Y cells into neurons. The magnetically controlled RA delivery resulted in the successful induction of neuronal differentiation with precise spatial and temporal control while minimizing reliance on complex microfluidic setups. Thus, the integration of magnetic actuation with supramolecular nanocarriers promotes new efficient routes and scalable protocols that go beyond state-of-the-art research in various bio-medical applications.

1. Introduction

Organoids have become an established tool in fundamental research and show vast potential for personalized regenerative medicine. However, they still lack the complex tissue micro-architecture of a living organ to become a physiologically relevant model.[1,2] To overcome the present limitations, an active line of research involves engineering functional materials and devices to guide organoid development *via* the controlled release of morphogens.[3] In tissue engineering, the spatio-temporal regulation of morphogen release is typically achieved using microfluidic devices[4–6] or *via* hydrogel modified microfluidics for morphogen delivery into planar cell-culture wells[7] or to 3D scaffolds.[8]

Micro- and nanoparticles have also been used to deliver morphogens by directly dosing them onto stem cell cultures,[9] but despite the efficacy of the method, this form of administration cannot offer precise spatial and temporal control.

Notably, magnetic nanoparticles (MNPs) are increasingly employed to manipulate biomolecules in microfluidic devices because of their unique properties of small size, responsiveness to external magnetic fields and the possibilities they offer for surface functionalization and binding to selected biomolecules.[10,11] Moreover, it has been recently demonstrated that devices consisting of properly shaped permanent magnets can efficiently confine MNPs within microfluidics and reliably move them within sub-millimeter channels across macroscopic distances (several tens of centimeters).[12,13] Such devices generate, along the longitudinal direction of a microchannel, high

[a] *National Research Council, Institute for Nanostructured Materials (CNR-ISMN), Via Pietro Gobetti 101, 40129 Bologna, Italy. E-mail: alessandro.surpi@cnr.it*
[b] *National Research Council, Institute for Nanostructured Materials (CNR-ISMN), URT of Messina at Department of Chemical, Biological, Pharmaceutical and Environmental Sciences (ChiBioFarAm), University of Messina, Viale F. Stagno d'Alcontres 31, 98166 Messina, Italy. E-mail: antonino.mazzaglia@cnr.it*
[c] *Dept. of Chemical, Biological, Pharmaceutical and Environmental Sciences (ChiBioFarAm), University of Messina, Viale F. Stagno d'Alcontres 31, 98166 Messina, Italy*
[d] *National Research Council, Institute for Microelectronics and Microsystems (CNR-IMM), SP Lecce-Monteroni Km 1,200, 73100 Lecce, Italy*
[e] *Center for Biomolecular Nanotechnologies, Istituto Italiano di Tecnologia, Arnesano 73010, Italy*
[f] *National Research Council, Institute for Nanostructured Materials (CNR-ISMN), Via Ugo La Malfa 153, 90146 Palermo, Italy*
[g] *Dept. of Chemical Sciences, University of Catania, Viale Andrea Doria 6, 95125 Catania, Italy*
† These authors contributed equally.

field gradients that strongly attract MNPs into a precisely defined region between the magnets where magnetic energy overcomes Brownian thermal motions, forming a ''magnetic trap''. The MNPs remain trapped therein even when the magnets are moved along the microchannel, as some of us have already reported.[12] Therefore, these devices enable a precise spatio-temporal control of MNP delivery and of morphogens they are linked to. In microfluidics, this could be a promising approach to guide organoid growth.

Still, the potential cytotoxicity of MNPs is a concern that needs to be addressed to develop a vector for morphogen delivery. Efforts are therefore being made to mitigate MNP toxicity through surface modifications[14] *via* biocompatible polymer coatings such as polyethylene glycol (PEG),[15,16] dextran[17–19] or polydopamine (PDA).[20,21] Emerging strategies to improve MNP's biocompatibility involve their combination with lipid membranes,[22,23] encapsulation into cell membranes[24] or extracellular vesicles.[25,26]

Beyond those approaches, supramolecular chemistry has been recognized as an important strategy to incorporate MNPs into host–guest assemblies, combining enhanced biocompatibility with designed responsiveness to external stimuli for, as an example, controlled drug release.[27]

In this regard, cyclodextrins (CDs) are especially suited for biotechnology applications because of their negligible toxicity and because their molecular structure (cyclic oligosaccharides) can be tailored to form complexes with a variety of guest molecules and inorganic nanoparticles.[28,29] Indeed, nanoassemblies based on cyclodextrins derivatized with amphiphilic portions can target tumoral cells and deliver chemotherapeutics[30] or photosensitisers[31] or guide cell adhesion.[32] Moreover, the encapsulation of MNPs into CD-based assemblies[33] or hydrogels has been exploited[34] to obtain fully biocompatible magnetic constructs for drug delivery[35] and biosensing.[36,37]

In this article, a supramolecular nanocarrier (SPION@SC6OH) for the delivery of retinoic acid (RA), composed of amphiphilic cyclodextrin assemblies (SC6OH) entangling superparamagnetic iron oxide nanoparticles (SPION) is presented and extensively characterized by thermogravimetric analysis (TGA), transmission electron microscopy (TEM), X-ray photoelectron spectroscopy (XPS) and photon correlation spectroscopy (PCS). Retinoic acid, the simplified term for all-*trans*-retinoic acid, is essential for embryonic development, bone growth regulation, and immune function[38] and represents a well-known differentiating agent used to generate neuronal-like cell lines.[39–41] We demonstrate that the RA-loaded nanocarrier (SPION@SC6OH/RA) can be steered through microfluidic channels by using external magnetic fields generated by a device based on actuated permanent magnets[12] to reliably deliver RA to *in vitro* cell cultures, where they induce differentiation of SH-5YSY cells into viable neurons. The developed nanocarrier fulfils the critical requirements for controlled delivery of morphogens: (i) biocompatibility and high dispersibility in aqueous/biological media as the nanocarrier surface is composed of oligosaccharides with very low or no toxicity, and the SPIONs interact with the assembly structure; (ii) chemically modifiable, as it is possible to chemically immobilize selected biomolecules or inorganic nanoparticles in the CD nanoassembly at a well-defined dose to induce cell differentiation; (iii) remotely steerable, as the SPIONs possess high-saturation magnetization that assures a robust and fast response to an external magnetic field.

2. Experimental section

2.1 Materials

Superparamagnetic iron oxide nanoparticles SPION (10 nm avg. particle size, 5 mg mL^{-1} in toluene), retinoic acid (RA), dichloromethane (DCM), chloroform and tetrahydrofuran (THF) were purchased from Sigma-Aldrich. Heptakis(2-*O*-(oligoethylene glycol)-6-hexylthio)-βCD, (SC6OH), with an average of 24 units of ethylene oxide (EO) and the most abundant peak at about 2935 Da, was synthesized *via* a slight modification of the general procedure.[42] All the solutions for spectroscopic characterizations were prepared in ultrapure water (S.A.L.F., Cenate Sotto, Bergamo, Italy).

2.2 Preparation of the magnetic nanoassemblies

The preparation of the magnetic supramolecular nanoassembly SPION@SC6OH/RA involves a two-step protocol involving both solvent evaporation and modified emulsion methods, as shown in Scheme 1.

Preparation of the SPION@SC6OH nanocarrier. A solution of SC6OH in chloroform was spontaneously evaporated overnight to form a thin film (~40 mg) that was then dissolved in THF. The resulting SC6OH solution was used to dissolve a thin film of SPIONs obtained from the overnight evaporation of a stock dispersion in toluene (4 mL, 5 mg mL^{-1}, ~20 mg). Pursuing a modified emulsion preparation method for supramolecular assemblies, the mixture was added dropwise to ultrapure water at 40 °C under magnetic stirring with a glass rod, then the THF was allowed to evaporate. After equilibration at room temperature, the SPION@SC6OH nanocarrier was purified from the unreacted material by magnetic settling for 2 h (neodymium permanent magnet, B = 398 mT, F = 63 kgf, size = 50.8 mm × 50.8 mm × 25.4 mm, MAGFINE SRL, Follonica, Italy) followed by centrifugation (15 min, 10 000 rpm). The precipitate was collected and washed with water, centrifuged, and dried under vacuum overnight. Additional SPIONs were retrieved from the supernatant by the same method. The recovery yield was calculated considering the final recovered amount of product (mg) *vs.* the sum of the initial weighed amount of each component.

Preparation of SPION@SC6OH/RA. 2 mg of SPION@SC6OH (SC6OH = 0.43 μmol, 63.9 wt% in cyclodextrin) were suspended in 100 μL of ultrapure water by vortex mixing for 10 min. The aqueous dispersion of SPION@SC6OH was used to hydrate a thin film of RA (2.45 μmol) that was previously prepared from the overnight evaporation of an amount (730 μL) of a stock solution in DCM (1 mg mL^{-1}), achieving an approximate 6 : 1 RA/SC6OH molar ratio. The mixture was vortex mixed for

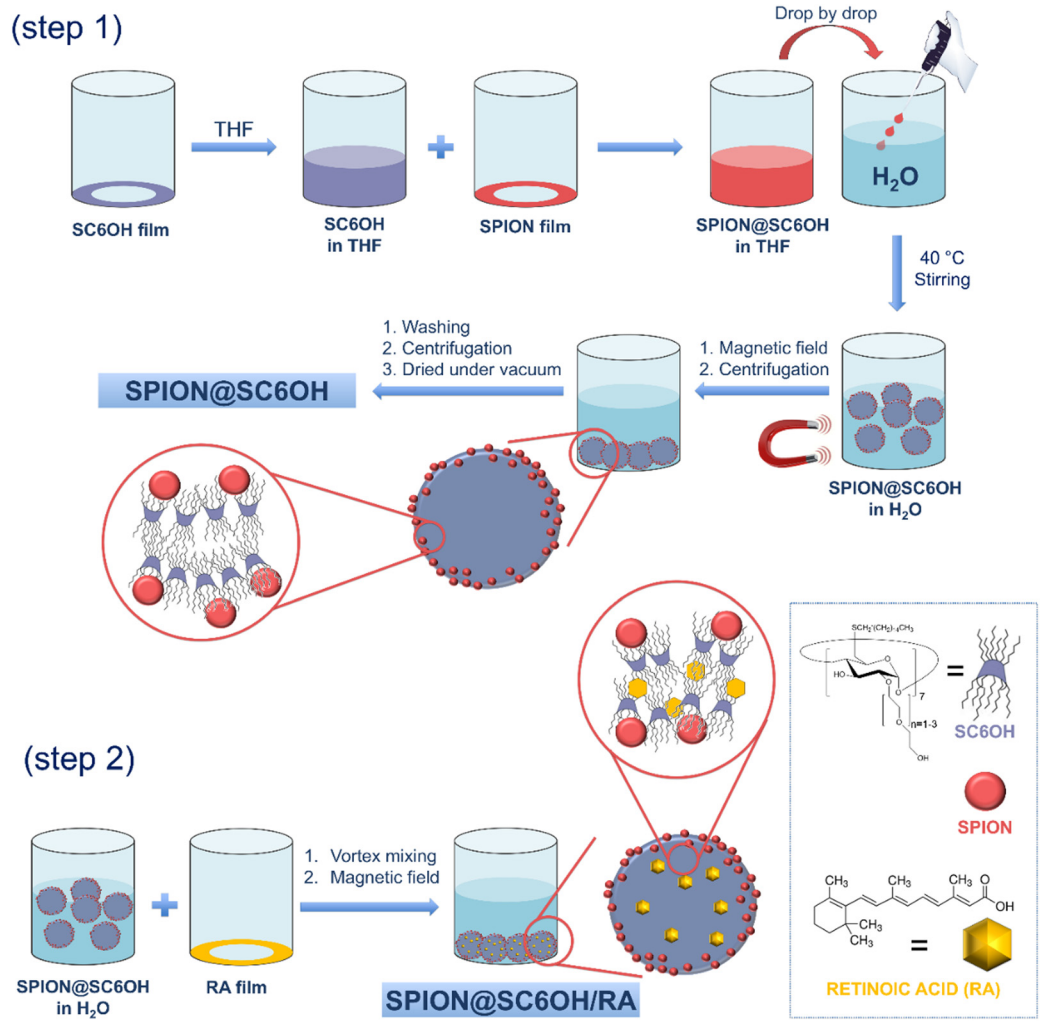

Scheme 1 Schematic depiction of the preparation of SPION@SC6OH (step 1) and SPION@SC6OH/RA (step 2) nanocarriers in an aqueous medium from the respective components.

15 minutes and purified as described above to obtain the SPION@SC6OH/RA assemblies.

The actual drug loading (DL), theoretical loading (TL) and entrapment efficiency (EE) were determined from eqn (1)–(3), respectively. The amounts of RA loaded into the nanoassemblies were estimated spectrophotometrically by using the extinction coefficient (ε) of RA calculated in DCM and evaluating the difference between the amount of RA initially added to formulations and the unloaded RA measured in the supernatant.

$$\mathrm{DL}\,(\%) = \frac{\text{Amount of RA in the nanoassemblies}}{\text{Weighted amount of nanoassembly}} \times 100 \quad (1)$$

$$\mathrm{TL}\,(\%) = \frac{\text{Amount of RA initially added to the nanoassemblies}}{\text{Weighted amount of nanoassembly}} \times 100 \quad (2)$$

$$\mathrm{EE}\,(\%) = \frac{\text{Amount of RA in the nanoassemblies}}{\text{Amount of RA initially added to the nanoassemblies}} \times 100 \quad (3)$$

2.3 Characterization of the magnetic nanocarrier

Thermogravimetric analysis (TGA). TGA was performed using a TAC 7/DX-equipped TGA 7 (PerkinElmer, Waltham, MA, USA) with a heating ramp of 10 °C min^{-1} in the temperature range 50–800 °C and a flux of dried air (60 mL min^{-1}).

UV/Vis spectroscopy. UV/Vis spectra were obtained with an Agilent 8453 UV-Vis spectrophotometer (Agilent Technologies, Santa Clara, CA, USA) in a 1 cm path length quartz cell. Molar extinction coefficient (ε) of RA in DCM at 366 nm was calculated from the interpolation of a standard calibration curve in the 87–261 μM range.

X-ray photoelectron spectroscopy (XPS). XPS spectra were acquired with an Escalab Mk II spectrometer, equipped with a standard Al Kα excitation source ($h\nu$ = 1486.6 eV) and a

five-channeltron detection system. The binding energy (BE) scale was calibrated by measuring the C 1s peak (BE = 285.0 eV) from the surface contamination. The accuracy of the BE measure was ±0.1 eV. Photoemission data were collected and processed with VGX900 and XPSPEAK4.1 software, respectively. Data analysis was performed by a nonlinear least square curve-fitting procedure with a properly weighted sum of Lorentzian and Gaussian component curves for the shape of the Voigt function, after Shirley background subtraction according to Sherwood.[43] Surface relative atomic concentrations were calculated by a standard quantification routine, including Wagner's energy dependence of attenuation length[44] and a standard set of VG Escalab sensitivity factors. The uncertainty of the atomic quantitative analysis is ±10%.

Photon correlation spectroscopy (PCS) analysis. The mean hydrodynamic diameter (D_H), width of distribution (polydispersity index, PDI), and ζ-potential of SC6OH and SPION@SC6OH were measured through photon correlation spectroscopy (PCS) with a Zetasizer Nano ZS (Malvern Instrument, Malvern, U.K.) equipped with a HeNe laser (P = 4.0 mW and λ = 633 nm). The measurements were performed at a 173° angle with respect to the incident beam at 25 ± 1 °C for each dispersion of SC6OH (40 μM) and SPION@SC6OH (0.17 mg mL^{-1}, [SC6OH] = 40 μM) at pH 7 using ultrapure water as dispersing medium. The deconvolution of the measured correlation curve to an intensity size distribution was achieved by using a non-negative least-squares algorithm. The results are reported as the mean of three separate measurements on three different batches ± the standard deviation (SD).

Stability studies. The colloidal stability of SPION@SC6OH was evaluated in ultrapure water by photon correlation spectroscopy. The aqueous dispersion was placed in a cuvette at 37 °C, acidified to pH 5.5 with hydrochloric acid, and monitored over the course of a week by measuring the D_H and ζ-potential of the nanoparticles. Each sample was analyzed in triplicate.

Transmission electron microscopy (TEM). For the TEM analysis, 7 μL of SPION (2 mg mL^{-1}) in toluene and SPION@SC6OH aqueous dispersion (2 mg mL^{-1}) were dropped onto a formvar-coated copper grid and left to settle for 30 min. Afterward, the excess liquid was removed using filter paper. No staining was applied to the obtained grids. TEM analysis was performed with a JEOL JEM-1011 transmission electron microscope at 100 kV operating voltage, equipped with a 7 megapixel CCD camera (Orius SC600A, Gatan, Pleasanton, CA). TEM image analysis was achieved with Gatan Digital Micrograph™ (DM) software.

2.4 Microfluidic apparatus for magnetic manipulation into miniaturized cell culture wells

The microfluidic chip is built on a 300 μm thick polydimethylsiloxane (PDMS) slab placed on a 25 × 75 mm^2 quartz microscope slide. The PDMS slab contains a 5 mm wide circular culture well (the bottom is formed by the quartz slide) and a 500 μm wide quartz capillary (immersed in the PDMS slab), which allows the passage of the nanocarrier SPION@SC6OH/RA to the culture well (Fig. S1). Externally, the capillary is connected with a medical-grade silicone tube (Silastic®, Dow Corning, Midland, MI, USA) through which the capillary can be filled with the nanocarriers and culture medium. Two 20 × 5 × 5 mm^3 NdFeB magnets with 1.3 T as remanence field (Supermagnete GmbH, Gottmadingen, Germany) are placed at a 5 mm edge-to-edge distance from each other. The microfluidic chip is positioned so that the capillary runs at the midpoint between the magnets and is orthogonal to the longest side of the magnets. The configuration has been designed by means of COMSOL simulations, defining the magnetic field generated by magnets with lateral sides from 2 to 10 mm and the respective magnetic forces on 10 nm large Fe_3O_4 nanoparticles. As shown previously,[12] the device generates a magnetic field and gradients able to confine magnetic nanoparticles between the magnets in a clepsydra-like shape about 200 μm wide. A motorized linear stage (Sigma Koki, TSDM 40-15, Tokyo, Japan) is used to move the magnets along the capillary. The stage is remotely operated *via* a single-axis stage controller (Sigma Koki, PAT-001, Tokyo, Japan) controlled by LabView software installed in an external computer. To ensure the optimal temperature, humidity, and O_2 and CO_2 concentrations for cell culture and differentiation, the microfluidic chip and the magnetic device are placed inside an incubator (Thermo Fisher Scientific Inc., Waltham, MA, USA) according to the experimental configuration shown in Fig. S2.

2.5 Cell culture and differentiation

Maintenance and differentiation of the human neuroblastoma cell line SH-SY5Y were carried out according to a published protocol[45] and only slight changes were introduced to optimize the neural differentiation in the microfluidic devices. Cells were cultured in 75 cm^2 flasks in Dulbecco's modified Eagle's medium – DMEM – (Merck KGaA, Darmstadt, Germany) and Ham's F-12 (Merck KGaA, Darmstadt, Germany) nutrient mixture (1 : 1) supplemented with 15% fetal bovine serum – FBS – (Merck KGaA, Darmstadt, Germany), 2 mM L-glutamine (Merck KGaA, Darmstadt, Germany), 100 U mL^{-1} penicillin (Merck KGaA, Darmstadt, Germany), and 100 mg mL^{-1} streptomycin (Merck KGaA, Darmstadt, Germany) at 37 °C and 5% CO_2. When the culture reached ∼80% confluence, the cells were trypsinized using trypsin–ethylenediaminetetraacetic acid (trypsin–EDTA) and seeded (25 000 cells per cm^2) in the culture well of the microfluidic device. After the time required for cell adhesion (4 h), differentiation was induced by replacing the medium with differentiation medium (DM) composed of DMEM F-12 Ham, 1× insulin/transferrin/selenium (ITS) (Merck KGaA, Darmstadt, Germany), 4 mM glutamine, 40 μg mL^{-1} gentamicin and 2.5 μg mL^{-1} amphotericin (DM). 10 μM RA was present only in the control experiments. After two days, the DM was replaced with DM containing 40 ng mL^{-1} neurotrophic brain-derived factor (BDNF). Half of the DM was changed daily by replacing it with fresh DM without any inducers until the end of the experiment. After 8 days of differentiation, the samples were characterized using the protocol of immunofluorescence staining of β-tubulin III co-labelling the nuclei with DAPI, as described by Chelli *et al.*[46] As a control, the same

differentiation protocol was applied in parallel to cells seeded on glasses placed in a 24-multiwell plate. In addition, cells were grown in the culture well of the microfluidic device in the presence of SPION@SC6OH (not RA loaded).

β-Tubulin III antibody staining. Class III β-tubulin is a widely used marker to assess neuronal differentiation[47] as it is exclusively expressed in neurons. Detailed steps for the staining protocol are reported below. Cultured cells were fixed with 4% paraformaldehyde in 1× PBS (phosphate buffer saline), pH 7.4 (Merck KGaA, Darmstadt, Germany) for 20 min at room temperature and then washed twice with 1× washing buffer. To permeabilize the cells, 0.1% Triton X-100 in 1× PBS was added, and left to react for 5 min at room temperature and then washed twice with 1× washing buffer. Blocking solution (BSA) and the primary antibody – anti-β-tubulin III (Merck KGaA, Darmstadt, Germany) – in the blocking solution were left for 30 min and 1 h, respectively, at room temperature and then washed three times with 1× wash buffer. The secondary antibody – Alexa fluor 594 (Merck KGaA, Darmstadt, Germany) – freshly diluted in 1× PBS was incubated for 60 min at room temperature and then washed three times with 1× washing buffer. Following this washing step, nuclei counterstaining was performed by incubating the cells with DAPI (4′,6-diamidino-2-phenylindole, Merck KGaA, Darmstadt, Germany) for 5 min at room temperature, followed by washing three times with 1× washing buffer. Fluorescence images were collected using a fluorescence microscope Nikon Eclipse I80 (Nikon Corp., Tokyo, Japan), equipped with a Nis-Elements F300 CCD camera (Nikon Corp., Tokyo, Japan).

Cell viability (resazurin reduction assay). The cell viability was determined by a resazurin reduction assay. Cells were seeded in the device with complete and differentiation medium and differentiation medium. After the incubation time, resazurin was added to the culture medium (10% v/v of medium in the device) and incubated for 3 h at 37 °C with 5% CO_2. Subsequently, aliquots from each sample were transferred to a 96 multiwell plate for fluorescence measurement (λ_{exc} 560 nm, λ_{em} 590 nm, Thermo Scientific Varioskan Flash Multimode Reader – Thermo Fisher Scientific Inc., Waltham, MA, USA). A negative control containing only the medium (without cells) was included to determine the background signal, and a positive control of 100% reduced resazurin (resofurin) reagent (without cells) was also introduced.

Statistical analysis. All data represented the mean ± standard deviation (SD) of independent culture experiments. Statistical significance was determined using one-way analysis of variance with Tukey's test for multiple comparisons using Origin 8 software (OriginLab Corporation). Differences were considered significant when $p < 0.005$ and $p < 0.001$.

3. Results and discussion

3.1 Magnetic nanocarrier preparation and characterization

SPION@SC6OH nanocarriers were prepared as an aqueous dispersion by the emulsion method (Scheme 1, step 1).[48] A mixed solution of SPION and SC6OH in THF was added dropwise to water under stirring. The magnetic nanocarrier was finally recovered (recovery yield ∼67%) by a combination of magnetic settling and centrifugation, followed by drying under vacuum. Thermogravimetric analysis was used to investigate the thermal oxidation behaviour of the nanocarriers (Fig. 1(A)). In particular, the organic moiety of the SPIONs shows a single degradation step at 164 °C with a residue at 800 °C of about 45.2%. On the other hand, the SC6OH shows a degradation step at 287 °C, followed by two minor ones at about 430 °C and 497 °C, leaving a residue at 800 °C of 1.1%. Finally, the SPION@SC6OH shows a first degradation step at 200 °C that could be attributed to the organic moieties of SPION, while the second and third degradation steps (at 322 °C and 463 °C, respectively) are attributable to the SC6OH counterpart. Comparing the SPION@SC6OH and SC6OH thermograms, the increased thermal degradation temperatures and the absence of weight loss at 497 °C might suggest a stabilization effect induced by the nanoparticles. Considering the residue at 800 °C of the SPION@SC6OH nanocarriers (16.3%), the loading of SC6OH was found to be 63.9%. Mean hydrodynamic diameter (D_H) and ζ-potential measurements were conducted to investigate the size and colloidal stability of SPION@SC6OH. The particle size analysis by PCS reveals a distribution profile dominated by a main broad population of about 250 nm (84% of intensity), accompanied by a less intense one around 20 nm (16% of the intensity). PCS measurements were compared with the size analysis of free SC6OH. Furthermore, in this case, we observed two families of nanoassemblies with a peak of lower intensity of ∼9 nm, with an amplitude of ∼7%, and a main peak with an intensity *ca.* 4-fold higher with a D_H of ∼250 nm (Fig. 1(B)). D_H values between SPION@SC6OH and SC6OH are comparable, but the latter displays a distribution profile with narrower peaks than for SPION@SC6OH. SC6OH presents a highly negative ζ-potential of −37 mV, which ensures the colloidal stability of the cyclodextrin nanoassemblies. A slight decrease in this value was observed in SPION@SC6OH, which exhibits a value of about −30 mV. In any case, these samples appear to be easily dispersible and exhibit good colloidal stability. The lower ζ-potential value and the broader size distribution profile observed for SPION@SC6OH with respect to SC6OH were tentatively ascribed to the partial formation of multiple-aggregates of magnetic nanoparticles interacting with SC6OH assemblies. The morphology of the SPION@SC6OH nanocarriers was investigated by TEM analysis (Fig. 2). Commercial hydrophobic SPION dispersed in toluene showed a quasi-spherical morphology, with an average diameter of 10.4 ± 1.8 nm, with no sign of aggregation. The analysis of the SPION@SC6OH showed a highly condensed core, due to an assembly of the amphiphilic cyclodextrin coated with a shell of SPION. Structures with an average size of about 300 nm, in agreement with PCS measurements, and other nearly micrometric aggregates, were present. Considering the nanocarrier fabrication process (Scheme 1, step 1), it is plausible to assume that the redispersion of SC6OH film in THF (which is a polar aprotic solvent) generated dense SC6OH pseudo-nanospheres

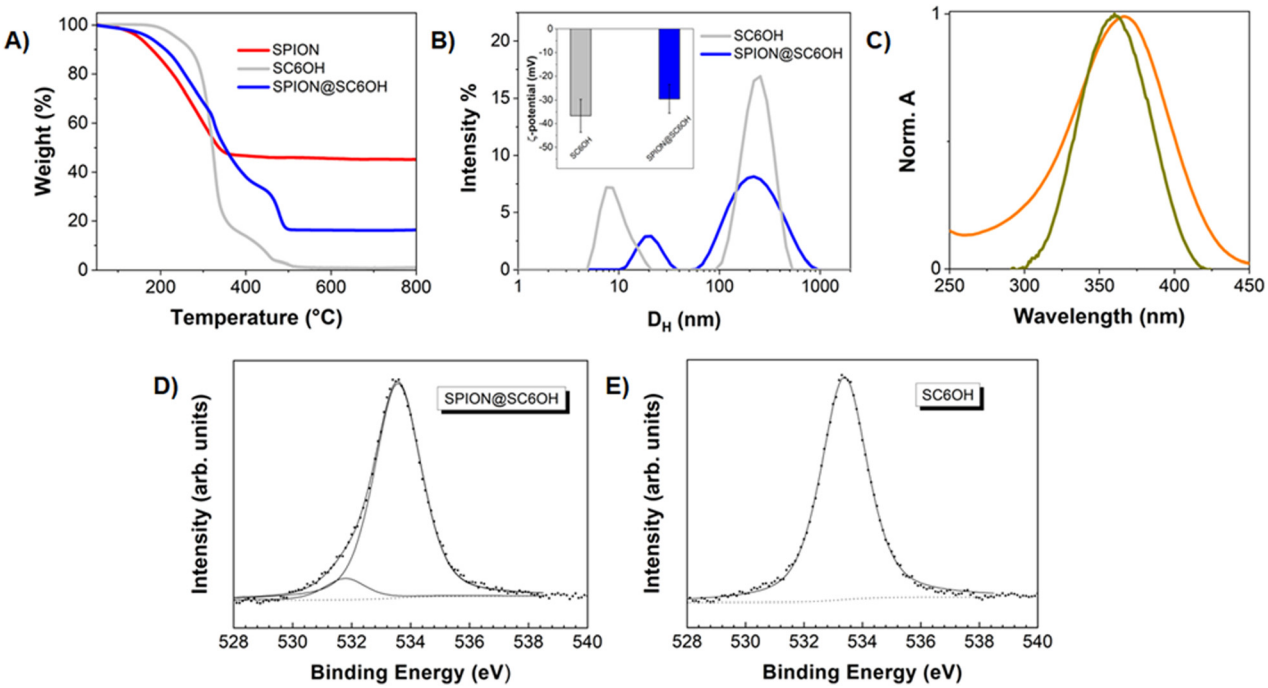

Fig. 1 (A) TGA thermograms of SPION, SC6OH, and SPION@SC6OH in an air atmosphere. (B) Mean hydrodynamic diameter (D_H) and ζ-potential ± SD (in the inset) of SC6OH (40 μM) and SPION@SC6OH in ultrapure water (0.17 mg mL^{-1}, [SC6OH] = 40 μM), pH 7. (C) Normalized UV/Vis absorption spectra of SPION@SC6OH/RA in ultrapure water (green line), and RA in DCM (orange line). (D) XPS curve-fitting of the O 1s spectrum of SPION@SC6OH. (E) XPS curve-fitting of the O 1s spectrum of SC6OH.

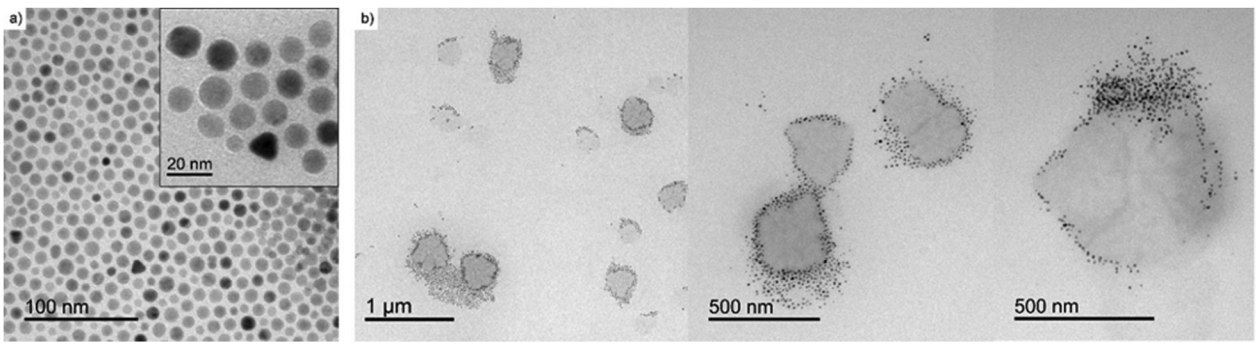

Fig. 2 TEM analysis of (a) SPIONs and (b) SPION@SC6OH.

stabilized in dispersion by the presence of the aliphatic tails of the amphiphilic cyclodextrin structure. In the next step, the suspension was used to redisperse the film of the hydrophobic magnetic nanoparticles SPION, which, by affinity, can partially intercalate in the aliphatic tails of the SC6OH. The magnetic separation used to perform the washing steps, and to facilitate the redispersion in water, can then be used to select the portion of the sample consisting of the SC6OH@SPION assemblies, which can be efficiently separated from the suspension due to the cumulative effect of the magnetization of the SPION trapped on the external surface of the SC6OH nanospheres. The amphiphilic nature of SC6OH guaranteed the correct dispersion of the system in water.

The results of the XPS analysis confirmed the presence of SPION on the surface of the SC6OH assembly.

Along with the main C 1s, O 1s and S 2p photoelectron signals shown in the XPS survey spectra of the investigated samples (Fig. S3), the presence of iron is detected on the surface of the SPION@SC6OH sample, as reported in Table 1.

Very similar C 1s spectra were recorded for the pure SC6OH and SPION@SC6OH samples, suggesting similar surface distributions of carbon species both before and after assembly of SC6OH with SPION (Fig. S4). The curve-fitting of the O 1s spectra of SPION@SC6OH and SC6OH, reported in Fig. 1(D) and (E), respectively, revealed a small component located at BE = 531.7 eV for SPION@SC6OH, which was ascribed to the presence of surface hydroxyl species, possibly FeO(OH).[49,50]

The presence of iron oxy-hydroxides FeO(OH) species on the surface of SPION is revealed both by the O1s and Fe $2p_{3/2}$ curve-fittings reported in Fig. S5. The curve-fitting of the Fe $2p_{3/2}$

Table 1 Surface chemical composition of the investigated samples by XPS. Elemental concentration is expressed as atomic percentage (at%)

Sample	C 1s	O 1s	S 2p	Fe 2p
SPIONs	90.8	6.2	—	3.0
SPION@SC6OH	88.7	9.9	1.0	0.4
SC6OH	92.1	7.2	0.7	—

spectrum of the SPIONs evidenced a peak component located at BE = 710.3 eV that can be assigned to iron oxides (Fe_2O_3, Fe_3O_4), and a component at BE = 711.3 eV can be attributed to surface iron oxy-hydroxides FeO(OH) species.[49–51] The highest binding energy peak at BE = 713 eV originates from the peak asymmetry observed in the Fe oxide band envelope.[52]

The colloidal stability of SPION@SC6OH was evaluated in ultrapure water at pH 5.5 and 37 °C by PCS. The relevant data are summarized in Table S1. The nanoparticles exhibited excellent stability in weakly acidic aqueous solution for one week, without showing any significant aggregation phenomena within 4 days. In more detail, the ζ-potential was approximately −34 mV and remained nearly constant over the course of one week. Similar to what was observed at neutral pH, the size distribution at pH 5.5 displayed two peaks at about 20 nm and 260 nm (Fig. 3(A)). As shown in Fig. 3(B), the size of SPION@SC6OH did not increase significantly within the first four days.

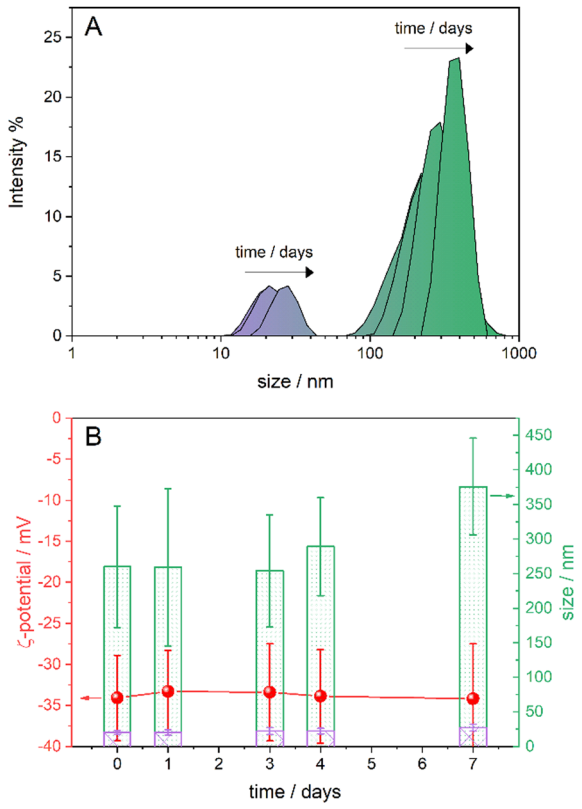

Fig. 3 (A) Size distribution of SPION@SC6OH nanoparticles (0.17 mg mL^{-1}, [SC6OH] = 40 μM) *vs.* time (arrows indicate changes from 1 to 7 days). (B) Mean hydrodynamic diameter (green and purple bars) and ζ-potential (red spheres) values ± SD *vs.* time at pH 5.5.

However, a notable increase of about 40% was observed after one week for both nanoparticle populations.

SPION@SC6OH/RA with a SC6OH/RA molar ratio of about 6 : 1 (Scheme 1, step 2) was prepared in aqueous solution by hydration of the organic film and sonication, according to a reported protocol (see the experimental section).[53] The final assembly was characterized by UV/Vis spectroscopy. After the purification (magnetic separation and centrifugation), the dispersion showed the presence of RA both in the supernatant and in the precipitate phases, as evidenced by the presence of its absorption band around 360 nm.

The lipophilic vitamin RA is almost insoluble and is chemically unstable in aqueous media. Therefore, the RA found in the supernatant – which contained the non-reacted materials – might be due to the presence of an excess of SC6OH that allows the RA to be carried into the aqueous dispersion. Both the absorption profiles of SPION@SC6OH/RA from redispersion of the precipitate phase and its supernatant exhibited an increase in the baseline. Spectra corrected for the scattering (Fig. S6) showed the excess of un-entrapped RA, which is likely dispersed in the supernatant by SC6OH assemblies not involved in the covering of SPION. The absorption spectrum of RA in DCM showed an absorption maximum at 366 nm. The UV/Vis spectra of SPION@SC6OH/RA (baseline corrected) in ultrapure water and RA in DCM were normalized for the maximum and are shown in Fig. 1(C). The two spectra were very similar but a hypsochromic shift (Δλ of 6 nm) was found for SPION@SC6OH/RA. The actual loading of RA into the nanoparticles was spectrophotometrically estimated using the extinction coefficient of RA in DCM that was previously calculated (λ = 366 nm, 3.3×10^4 M^{-1} cm^{-1}, Fig. S7) and determined by the difference of the weighted amount of RA initially present in organic film and those obtained after the dissolution in DCM of the supernatant that was collected and dried under vacuum. The actual loading of RA within SPION@SC6OH, calculated from eqn (1), was about 1.7% and the entrapment efficiency, calculated from eqn (3), was about 6.4%.

3.2 Magnetically controlled release of morphogenic RA into cell cultures

Having demonstrated that SPION@SC6OH/RA can be reliably produced, we investigated whether they can be magnetically manipulated, steered through microfluidic channels and used to deliver the morphogen to *in vitro* cell cultures. With this aim, an experimental model device was developed (described in the experimental section) to test the magnetically enabled injection of SPION@SC6OH/RA into miniaturized cell culture wells. Despite its simplicity, the system represents a model for a microfluidic chip as it recapitulates the basic elements as a compartment for cell culture and a microfluidic channel for dosing biochemicals to the cells. SPION@SC6OH/RA are magnetically actuated through the capillary and into the culture well by a magnetic tool composed of a couple of permanent magnets arranged as described previously.[12]

The magnetic tool, shown in Fig. 4, is critical for morphogen injection because it enables the separation of the

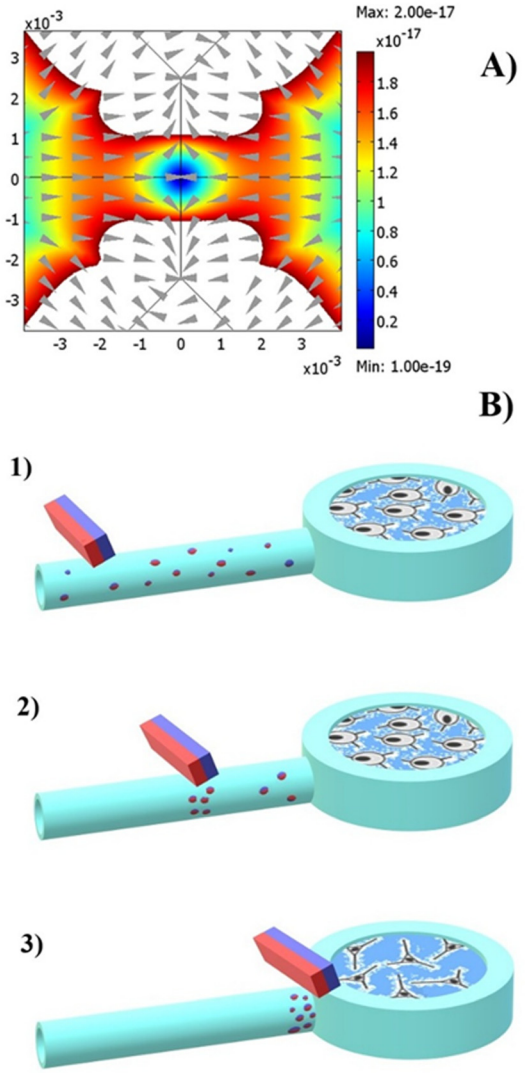

Fig. 4 (A) Numerical simulation of the magnetic force acting on SPIONs. The arrows represent the direction of the magnetic force, while the false-colour map represents the intensity. For clarity, the intensity is not shown in regions far from the capillary (white zone), where the intensity is higher but does not affect the SPION@SC6OH/RA nanosystem as they are physically constrained inside the capillary. (B) Scheme of the magnetic manipulation of SPION@SC6OH/RA (see the main text for further details).

SPION@SC6OH/RA nanosystem from the aqueous solution into a dense plug situated between the magnets, the subsequent controlled transport through the capillary to cell culture well and, finally, the delivery of RA into the culture well at the right concentration to act as differentiating agent for the neuronal cell line.[54]

This tool acts as a "magnetic trap" for this magnetic nanosystem. Fig. 4(A) shows the distribution of the magnetic forces acting on the SPIONs; the false-color map accounts for the intensity, while the arrows indicate the force direction. The magnetic force reaches a maximum of 2×10^{-17} N at about ± 2 mm from the center (defined as the intersection point of the capillary axis and the line connecting the edges of the magnets) and steadily decreases with distance. The direction of the magnetic force along the capillary axis is parallel to it and points towards the center of the device. This ensures that the SPION@SC6OH/RA that are initially dispersed in the capillary are efficiently dragged towards the area between the magnets. Moreover, once a magnetic nanoparticle reaches that area, it cannot escape because the magnetic force continuously redirects it toward this point. Magnetic energy calculations reported by Surpi *et al.*[12] for the same magnetic configuration also show that, in this device, the magnetic energy exceeds the thermal energy of such nanoparticles, preventing their escape due to Brownian motion, so that an effective magnetic confinement of SPION@SC6OH/RA nanosystem is assured. These magnetic aggregates are effectively trapped by the device and, crucially for this application, solidly follow the magnet's movement along the capillary.[12] In the following discussion, the different phases of the process are indicated by the numbers shown in Fig. 4(B). At the beginning of the experiment, the cell medium solution fills both the capillary and the cell culture well, where cells are seeded in the embryonic stage. At this stage, SPION@SC6OH/RA nanosystems are uniformly dispersed in a portion of the silicone tube and divided from the rest of the fluid by a small air gap to avoid intermixing. Then, the nanoparticle-containing solution was injected by using a peristaltic pump with a flow rate of 30 μL min^{-1} into the quartz capillary. The injection was done with the magnetic tool kept at the capillary-silicon tube connection. After the capillary was filled, the SPION@SC6OH/RA system was allowed to concentrate for around 10 min between the magnets (1). A back-and-forth run at 30 μm s^{-1} was then done by the magnets to sweep the entire capillary length and capture the SPION@SC6OH/RA nanosystems that were not initially trapped between the magnets. The speed of the magnets was chosen so that it sits in the middle of the "stability window", as previously reported,[12] where the magnetic nanoparticles can solidly follow the movement of the external magnets (2). Finally, by moving the magnets at 30 μm s^{-1}, a concentrated plug of SPION@SC6OH/RA is delivered to the outlet of the capillary, where it connects to the culture well (3).

3.3 Induced differentiation of SH-SY5Y cells into neuron cells

The supramolecular magnetic SPION@SC6OH/RA nanoassemblies showed morphogenic capability by controlling the differentiation of human neuroblastoma cells SH-SY5Y into a differentiated human neuron-like phenotype in the miniaturized well of the microfluidic device described above. The cell culturing and differentiation protocol of Shipley *et al.*[45] was adapted to our experimental setup with only slight modifications. The phenotypic characteristics of the cells were evaluated by microscopic inspection. Morphology and staining patterns, such as DAPI and the indirect immunofluorescence detection of neuronal class III β-tubulin (primary antibody: anti-β-tubulin III, secondary antibody: Alexa fluor 594), were exploited. As seen in Fig. 5(A), initially (a) the SH-SY5Y cells appear small and round, and feature prominent and uniform (in shape and size) nuclei. As the differentiation process begins (b), the cells lose

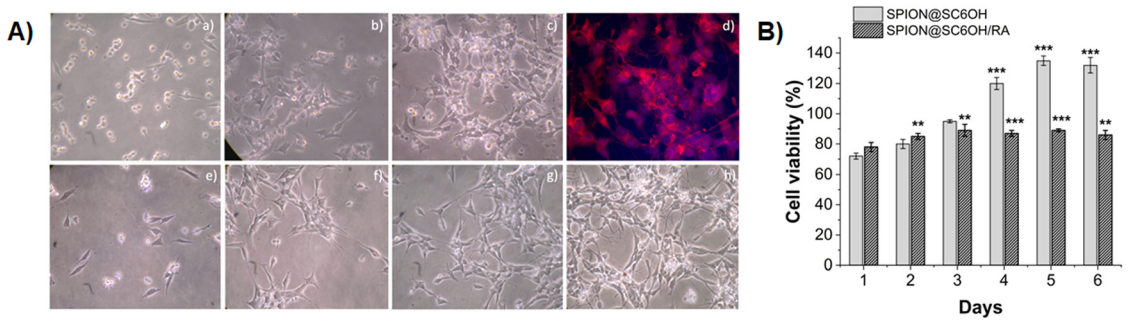

Fig. 5 (A) Differentiation of SH-SY5Y cells into neuron-like phenotype induced by the RA released from SPION@SC6OH/RA: (a)–(c) bright-field images from different differentiation steps into the miniaturized culture well of the custom microfluidic device, from day 1 to day 7; (d) fluorescence microscopy image of differentiated SH-SY5Y cells cultured on the custom microfluidic device and labelled with DAPI (blue colour, nuclear staining) and with class III β-tubulin immunostaining (red colour, neuron-associated cytoskeletal protein), day 7; (e)–(h) bright-field images from control experiments in which free RA was added to conventional cell cultures, from day 1 to day 7; (B) viability graph of SH-SY5Y cell culture on the miniaturized culture well of the custom microfluidic device treated with the empty SPION@SC6OH nanocarrier and SPION@SC6OH/RA; data are represented by the mean value ± standard deviation. Statistical analysis was performed using ANOVA followed by Tukey's test $^{**}p < 0.005$ and $^{***}p < 0.001$ denotes significant differences with respect to control (day 1).

their round shape and begin to elongate, becoming spindle-shaped to resemble neuronal progenitor cells. Moreover, they cluster in rosette-like structures that are the typical hallmark of neuronal progenitor cells in culture. As the cells continue to differentiate, they assume characteristic neuron-like shapes (c) as they grow long and thin projections, which will eventually develop into axons and dendrites. The culture itself changes its overall appearance as it adopts web-like structures as individual cells extend their axon- and dendrite-like extensions. Not surprisingly, the differentiation stages are clearer in the control experiment (e–f–g–h), where free RA – without the SPION@SC6OH nanocarrier – was added into a conventional cell culture, according to the Shipley *et al.* protocol.[45] In addition, from the fluorescence microscopy image (d), clear branching of the cells was confirmed by the indirect immunofluorescence assay for the specific neuron-associated cytoskeletal marker anti-β-tubulin.

Fig. 5(B) shows the viability patterns of both SPION@SC6OH and SPION@SC6OH/RA treated SH-SY5Y cell cultures in the custom microfluidic apparatus of this work. The viability of the cells reflects the growth rate and mirrors the key stages of differentiation. As a tumoral cell line, SH-SY5Y continuously proliferates while their differentiation – that is induced by the addition of RA[55] – leads to a decrease in proliferation rate[56] a distinct pattern in the growth curve of cell viability for the cell culture treated with magnetically delivered RA that mirrors key stages of differentiation as the growth rate of the cell population changes during different development phases. In the first phase (up to 3 days), the curve shows an upward trend as SH-SY5Y cells rapidly proliferate in their undifferentiated state. After 3 days, the viability reached a plateau due to the commitment of SH-SY5Y in the RA-induced differentiation to neuron-like phenotype, which reduced the overall proliferation rate. This profile was maintained until the end of the experiment on day 6. Apparently, the cells are now committed to the specific neuronal lineage and do not keep proliferating as undifferentiated stem cells. Moreover, as the cells remain largely viable (the curve does not decrease), this demonstrates that the device provides an optimal environment in which the cells remain healthy. In contrast, in the control experiment, where the cell culture was dosed with SPION@SC6OH nanocarriers lacking RA, the growth curve shows a steep upward trend for the entire period, indicating that the cells remain in a proliferative state and keep dividing rapidly. The growth seems to slow down on day 6, probably because the cell density became too high and the cells started to feel stress because of the limited space of the culture well.

Overall, the application described here encompasses the development of a magnetic nanocarrier for the delivery of biologically active molecules as morphogen(s) and its control *via* "magnetic trap" methodology to decouple its delivery from the fluid flow necessary for nutrients feeding and waste removal. We are aware that the experiment was carried out in a simplified model. Still, it recapitulates the functions needed for guided organoid development, and the technology presented here can be easily engineered into more complex devices. While the presented research consists of a proof-of-principle application focused on RA delivery, the results can be easily extended on two fronts: (1) using other biomolecules as morphogens and (2) using more complex geometries for culture wells. Indeed, virtually any other molecular morphogen can be embedded in the cyclodextrin supramolecular construct, thus providing a modular tool for complex tissue engineering. Also, the "magnetic trap" method used here can be adapted to the more complex microfluidics required to grow fully developed tissues or organs and to deliver different morphogens following a timely, ordered schedule. On the other hand, the "magnetic trap" device can, in principle, steer MNPs through a dish without any need for microfluidics as the couple of magnets employed generates a field that efficiently traps the MNPs in the plane between them. A physical constraint is still needed in the transverse direction to prevent MNPs from attaching to the magnet surface. This opens the tantalizing possibility of guiding the release of morphogens directly in a dish. Therefore, this

technology enables the spatially and temporally controlled delivery of morphogens throughout the entire tissue development and could replicate natural developmental gradients to build bioengineered organoids closely mimicking the cell diversity and the microarchitecture of *in vivo* organs. Its simplicity, flexibility, and scalability make it an ideal experimental platform for a number of cutting-edge issues in developmental biology, such as the formation of vascularized tissues,[57–59] brain regionalization,[60] or liver zonation.[61] It can also be used to study morphogenetic processes *in vitro*, shedding light on how gradients orchestrate patterning in embryos.[62] Finally, in the field of regenerative medicine, it could be integrated into recently proposed microfluidic platforms to culture patient-derived organoids.[63]

4. Conclusions

This work demonstrates that a supramolecular assembly based on a biocompatible cyclodextrin-based nanoconstruct hosting superparamagnetic iron oxide nanoparticles (SPION@SC6OH) and retinoic acid (RA) can be magnetically steered through microfluidic environments and control the differentiation of SH-SY5Y cells cultured in miniaturized compartments. The possibility for the nanoparticles to be actuated by external magnets allows for a spatially and temporally controlled release of morphogens. In turn, this will enable novel engineering approaches to dynamically control organoid formation over time and, ultimately, lead to better models of human tissue. In organoid research, magnetic actuation has been used to assemble magnetic-nanoparticle-laden cells into a 3D model of tissues or gland-like constructs. Here, instead, we demonstrate a proof-of-principle experiment in which cell-differentiating agents are delivered *via* magnetic nanoassembly. To our knowledge, this is the first demonstration of morphogen delivery using magnetically actuated magnetic nanoparticles, opening new avenues for magnetic tissue engineering in organoid research with ramifications in neuronal repair, immune modulation, bone regeneration, and beyond.

Author contributions

Alessandro Surpi: methodology, investigation, data curation, writing – original draft, project administration, funding acquisition, conceptualization; Roberto Zagami: methodology, investigation, data curation, visualization; Marianna Barbalinardo: methodology, investigation, data curation, visualization, writing – original draft; Nina Burduja: methodology, investigation; Giuseppe Nocito: review & editing, visualization; Riccardo Di Corato: methodology, investigation, data curation; Maria Pia Casaletto: methodology, investigation, data curation, writing – review & editing; Francesco Valle: investigation, discussion; Angelo Nicosia: methodology, investigation, data curation, visualization; Placido Mineo: methodology, investigation, data curation, writing – review & editing; Valentin Alek Dediu: writing – original draft, project administration, funding acquisition, conceptualization; Antonino Mazzaglia: writing – original draft, supervision, project administration, funding acquisition, supervision, conceptualization.

Conflicts of interest

There are no conflicts to declare.

Data availability

The data supporting this article have been included as part of the SI. Supplementary information: Plan view of the microfluidic chip (Fig. S1); experimental set up configuration for magnetically controlled delivery of SPION/SC6OH/RA (Fig. S2); XPS survey spectra of the investigated samples (Fig. S3); XPS curve-fitting of C 1s spectra of the investigated samples (Fig. S4); Fe $2p_{3/2}$ and O 1s XPS curve-fitting in the SPION sample (Fig. S5); DLS results on SPION@SC6OH (Table S1); UV/Vis spectra of the aqueous dispersions of SPION@SC6OH/RA (Fig. S6); absorption calibration curve for retinoic acid in DCM (Fig. S7). See DOI: **https://doi.org/10.1039/d5ma00374a**

Acknowledgements

Instrumentation and operating expenses for this research have been mainly funded by the MADMAN+ project – ISMN-CNR programme for scientific projects led by early-stage researchers – CNR Protocol Identification Number: 0001367. Grants and personnel costs were covered by the European Union Horizon 2020 research and innovation programme under the projects MADIA (MAgnetic DIagnostic Assay for neurodegenerative disease) grant agreement no. 732678 and BOW (Biogenic Organotropic Wetsuits) grant agreement no. 952183 and by the Italian National Recovery and Reliance Plan (PNRR), part of the European Union NextGenerationEU programme, under the projects ECOSISTER (ECOSystem for sustainable transition of Emilia-Romagna) ECS 00000033 and SAMOTHRACE (SiciliAn MicrOnanoTecH Research And innovation Center) ECS 00000022. The authors thank Tatiana Shelyakova for the key suggestions on the magnetic configuration, Vincenzo Ragona for technical assistance, Alberto Riminucci for software development, Massimiliano Cavallini for illuminating discussions and Milo Malanga (CarboHyde, Budapest) for providing the amphiphilic cyclodextrin. Michele Muccini deserves a distinct acknowledgment for funding acquisition.

Notes and references

1 M. Hofer and M. P. Lutolf, *Nat. Rev. Mater.*, 2021, **6**, 402–420.
2 M. M. A. Verstegen, R. P. Coppes, A. Beghin, P. De Coppi, M. F. M. Gerli, N. de Graeff, Q. Pan, Y. Saito, S. Shi, A. A. Zadpoor and L. J. W. van der Laan, *Nat. Med.*, 2025, **31**, 409–421.

3 C. R. Marti-Figueroa and R. S. Ashton, *Acta Biomater.*, 2017, **54**, 35–44.
4 I. Koh and M. Hagiwara, *Commun. Biol.*, 2023, **6**, 299.
5 C. Quílez, E. Y. Jeon, A. Pappalardo, P. Pathak and H. E. Abaci, *Adv. Healthcare Mater.*, 2024, **13**, 2400405.
6 P. Samal, C. van Blitterswijk, R. Truckenmüller and S. Giselbrecht, *Adv. Mater.*, 2019, **31**, 1805764.
7 S. Cosson and M. P. Lutolf, *Sci. Rep.*, 2014, **4**, 4462.
8 B. O'Grady, D. A. Balikov, J. X. Wang, E. K. Neal, Y.-C. Ou, R. Bardhan, E. S. Lippmann and L. M. Bellan, *Biomater. Sci.*, 2019, **7**, 1358–1371.
9 A. M. Bratt-Leal, A. H. Nguyen, K. A. Hammersmith, A. Singh and T. C. McDevitt, *Biomaterials*, 2013, **34**, 7227–7235.
10 A. van Reenen, A. M. de Jong, J. M. J. den Toonder and M. W. J. Prins, *Lab Chip*, 2014, **14**, 1966–1986.
11 K. Wu, D. Su, J. Liu, R. Saha and J.-P. Wang, *Nanotechnology*, 2019, **30**, 502003.
12 A. Surpi, T. Shelyakova, M. Murgia, J. Rivas, Y. Piñeiro, P. Greco, M. Fini and V. A. Dediu, *Sci. Rep.*, 2023, **13**, 5301.
13 A. Surpi, M. Murgia, S. López-Amoedo, M. A. González-Gómez, Y. Piñeiro, J. Rivas, V. Perugini, M. Santin, T. Sobrino, P. Greco, F. Campos and V. A. Dediu, *J. Nanobiotechnol.*, 2023, **21**, 329.
14 E. V. Araújo, S. V. Carneiro, D. M. A. Neto, T. M. Freire, V. M. Costa, R. M. Freire, L. M. U. D. Fechine, C. S. Clemente, J. C. Denardin, J. C. S. dos Santos, R. Santos-Oliveira, J. S. Rocha and P. B. A. Fechine, *Adv. Colloid Interface Sci.*, 2024, **328**, 103166.
15 M. M. Yallapu, S. P. Foy, T. K. Jain and V. Labhasetwar, *Pharm. Res.*, 2010, **27**, 2283–2295.
16 L. Sun, C. Huang, T. Gong and S. Zhou, *Mater. Sci. Eng., C*, 2010, **30**, 583–589.
17 C. Tassa, S. Y. Shaw and R. Weissleder, *Acc. Chem. Res.*, 2011, **44**, 842–852.
18 Q. Hu, Y. Lu and Y. Luo, *Carbohydr. Polym.*, 2021, **264**, 117999.
19 J. S. Basuki, A. Jacquemin, L. Esser, Y. Li, C. Boyer and T. P. Davis, *Polym. Chem.*, 2014, **5**, 2611–2620.
20 M. Wu, D. Zhang, Y. Zeng, L. Wu, X. Liu and J. Liu, *Nanotechnology*, 2015, **26**, 115102.
21 M. Romano, M. A. González Gómez, P. Santonicola, N. Aloi, S. Offer, J. Pantzke, S. Raccosta, V. Longo, A. Surpi, S. Alacqua, G. Zampi, V. A. Dediu, B. Michalke, R. Zimmerman, M. Manno, Y. Piñeiro, P. Colombo, E. Di Schiavi, J. Rivas, P. Bergese and S. Di Bucchianico, *ACS Biomater. Sci. Eng.*, 2023, **9**, 303–317.
22 M.-S. Martina, J.-P. Fortin, C. Ménager, O. Clément, G. Barratt, C. Grabielle-Madelmont, F. Gazeau, V. Cabuil and S. Lesieur, *J. Am. Chem. Soc.*, 2005, **127**, 10676–10685.
23 M. Mendozza, L. Caselli, A. Salvatore, C. Montis and D. Berti, *Soft Matter*, 2019, **15**, 8951–8970.
24 G.-T. Yu, L. Rao, H. Wu, L.-L. Yang, L.-L. Bu, W.-W. Deng, L. Wu, X. Nan, W.-F. Zhang, X.-Z. Zhao, W. Liu and Z.-J. Sun, *Adv. Funct. Mater.*, 2018, **28**, 1801389.
25 G. Jia, Y. Han, Y. An, Y. Ding, C. He, X. Wang and Q. Tang, *Biomaterials*, 2018, **178**, 302–316.
26 L. Yang, K. D. Patel, C. Rathnam, R. Thangam, Y. Hou, H. Kang and K.-B. Lee, *Small*, 2022, **18**, 2104783.
27 Q.-D. Hu, G.-P. Tang and P. K. Chu, *Acc. Chem. Res.*, 2014, **47**, 2017–2025.
28 G. Chen and M. Jiang, *Chem. Soc. Rev.*, 2011, **40**, 2254–2266.
29 A. Pandey, *Environ. Chem. Lett.*, 2021, **19**, 4297–4310.
30 M. L. Bondì, A. Scala, G. Sortino, E. Amore, C. Botto, A. Azzolina, D. Balasus, M. Cervello and A. Mazzaglia, *Biomacromolecules*, 2015, **16**, 3784–3791.
31 R. Zagami, G. Sortino, E. Caruso, M. C. Malacarne, S. Banfi, S. Patanè, L. Monsù Scolaro and A. Mazzaglia, *Langmuir*, 2018, **34**, 8639–8651.
32 F. Valle, S. Tortorella, A. Scala, A. Cordaro, M. Barbalinardo, F. Biscarini and A. Mazzaglia, *Nanoscale Adv.*, 2020, **2**, 5897–5904.
33 J. H. Schenkel, A. Samanta and B. J. Ravoo, *Adv. Mater.*, 2014, **26**, 1076–1080.
34 B. P. Nowak and B. J. Ravoo, *Faraday Discuss.*, 2019, **219**, 220–228.
35 M. Trapani, A. Cordaro, R. Zagami and A. Mazzaglia, in *Supramolecular Nanotechnology: Advanced Design of Self-Assembled Functional Materials*, ed. O. Azzaroni and M. Conda-Sheridan, Wiley-VCH GmbH., 1st edn, 2023, ch. 29, pp. 795–819.
36 J. Muñoz, N. Crivillers, B. J. Ravoo and M. Mas-Torrent, *Nanoscale*, 2020, **12**, 9884–9889.
37 A. Mazzaglia, G. Di Natale, R. Tosto, A. Scala, G. Sortino, A. Piperno, M. P. Casaletto, A. Riminucci, M. L. Giuffrida, P. G. Mineo, V. Villari, N. Micali and G. Pappalardo, *J. Colloid Interface Sci.*, 2022, **613**, 814–826.
38 J. A. Hall, J. R. Grainger, S. P. Spencer and Y. Belkaid, *Immunity*, 2011, **35**, 13–22.
39 J. Rohwedel, K. Guan and A. M. Wobus, *Cells Tissues Organs*, 1999, **165**, 190–202.
40 N. Bayeva, E. Coll and O. Piskareva, *J. Pers. Med.*, 2021, **11**, 211.
41 A. Nicosia, G. La Perna, L. M. Cucci, C. Satriano and P. Mineo, *Polymers*, 2022, **14**, 4329.
42 R. Zagami, A. Barattucci, L. Monsù Scolaro, M. Viale, G. Raffaini, P. Maria Bonaccorsi and A. Mazzaglia, *J. Mol. Liq.*, 2023, **389**, 122841.
43 P. M. A. Sherwood, D. Briggs and M. P. Seah, *Data Analysis in X-ray Photoelectron Spectroscopy in Practical Surface Analysis by Auger and X-ray Photoelectron Spectroscopy*, New York, 1990.
44 C. D. Wagner, L. E. Davis and W. M. Riggs, *Surf. Interface Anal.*, 1980, **2**, 53–55.
45 M. M. Shipley, C. A. Mangold and M. L. Szpara, *J. Vis. Exp.*, 2016, 11, DOI: **10.3791/53193**.
46 B. Chelli, M. Barbalinardo, F. Valle, P. Greco, E. Bystrenova, M. Bianchi and F. Biscarini, *Interface Focus*, 2014, **4**, 20130041.
47 J. Guo, C. Walss-Bass and R. F. Ludueña, *Cytoskeleton*, 2010, **67**, 431–441.
48 R. Abazari, A. R. Mahjoub and S. Sanati, *J. Mol. Liq.*, 2016, **223**, 1133–1142.

49 C. D. Wagner, A. V. Naumkin, A. Kraut-Vass, J. W. Allison, C. J. Powell and J. R. Rumble Jr., *NIST Standard Reference Database 20, Version 3.4*, 2003.
50 M. P. Casaletto, V. Figà, A. Privitera, M. Bruno, A. Napolitano and S. Piacente, *Corros. Sci.*, 2018, **136**, 91–105.
51 J. F. Moulder, W. F. Stickle, P. E. Sobol, K. D. Bomben, J. Chastain and R. C. King Jr., *Handbook of X-Ray Photoelectron Spectroscopy, Physical Electronics*, Inc, USA, Eden Prairie, MN, 1995.
52 A. Bozzi, T. Yuranova, J. Mielczarski and J. Kiwi, *New J. Chem.*, 2004, **28**, 519–526.
53 R. Zagami, V. Rapozzi, A. Piperno, A. Scala, C. Triolo, M. Trapani, L. E. Xodo, L. Monsù Scolaro and A. Mazzaglia, *Biomacromolecules*, 2019, **20**, 2530–2544.
54 B. A. Pawson, C. W. Ehmann, L. M. Itri and M. I. Sherman, *J. Med. Chem.*, 1982, **25**, 1269–1277.
55 G. Melino, C. J. Thiele, R. A. Knight and M. Piacentini, *J. Neuro-Oncol.*, 1997, **31**, 65–83.
56 J. Kovalevich and D. Langford, in *Neuronal Cell Culture: Methods and Protocols*, ed. S. Amini and M. K. White, Humana Press, Totowa, NJ, 2013, pp. 9–21.
57 R. A. Wimmer, A. Leopoldi, M. Aichinger, N. Wick, B. Hantusch, M. Novatchkova, J. Taubenschmid, M. Hämmerle, C. Esk, J. A. Bagley, D. Lindenhofer, G. Chen, M. Boehm, C. A. Agu, F. Yang, B. Fu, J. Zuber, J. A. Knoblich, D. Kerjaschki and J. M. Penninger, *Nature*, 2019, **565**, 505–510.
58 O. J. Abilez, H. Yang, Y. Guan, M. Shen, Z. Yildirim, Y. Zhuge, R. Venkateshappa, S. R. Zhao, A. H. Gomez, M. El-Mokahal, L. Dunkenberger, Y. Ono, M. Shibata, P. N. Nwokoye, L. Tian, K. D. Wilson, E. H. Lyall, F. Jia, H. T. Wo, G. Zhou, B. Aldana, I. Karakikes, D. Obal, G. Peltz, C. K. Zarins and J. C. Wu, *Science*, 2025, **388**, 1038–1044.
59 Y. Miao, N. M. Pek, C. Tan, C. Jiang, Z. Yu, K. Iwasawa, M. Shi, D. O. Kechele, N. Sundaram, V. Pastrana-Gomez, D. I. Sinner, X. Liu, K. C. Lin, C.-L. Na, K. Kishimoto, M.-C. Yang, S. Maharjan, J. Tchieu, J. A. Whitsett, Y. S. Zhang, K. W. McCracken, R. J. Rottier, D. N. Kotton, M. A. Helmrath, J. M. Wells, T. Takebe, A. M. Zorn, Y.-W. Chen, M. Guo and M. Gu, *Cell*, 2025, **188**, 1–19.
60 Y. Zhu, X. Zhang, L. Sun, Y. Wang and Y. Zhao, *Adv. Mater.*, 2023, **35**, 2210083.
61 H. A. Reza, C. Santangelo, K. Iwasawa, A. A. Reza, S. Sekiya, K. Glaser, A. Bondoc, J. Merola and T. Takebe, *Nature*, 2025, **641**, 1258–1267.
62 S. Sun, Z. Zhou, A. Tang and J. Fu, *Curr. Opin. Biomed. Eng.*, 2025, **35**, 100605.
63 J. C. Means, A. L. Martinez-Bengochea, D. A. Louiselle, J. M. Nemechek, J. M. Perry, E. G. Farrow, T. Pastinen and S. T. Younger, *Nature*, 2025, **638**, 237–243.